Cryo-EM structure of the yeast TREX complex and coordination with the SR-like protein Gbp2

Yihu Xie[a,*], Bradley P. Clarke[a], Yong Joon Kim[b,c], Austin L. Ivey[a], Pate S. Hill[a], Yi Shi[b,c], and Yi Ren [a,*]

[a] Department of Biochemistry, Vanderbilt University School of Medicine, Nashville, TN, USA;
[b] Department of Cell Biology, University of Pittsburgh, Pittsburgh, PA, USA.
[c] Medical Scientist Training Program, University of Pittsburgh and Carnegie Mellon University, Pittsburgh, PA, USA

*Correspondence to: yihu.xie@vanderbilt.edu or yi.ren@vanderbilt.edu

Abstract

The evolutionarily conserved TREX complex plays central roles during mRNP (messenger ribonucleoprotein) maturation and export from the nucleus to the cytoplasm. In yeast, TREX is composed of the THO sub-complex (Tho2, Hpr1, Tex1, Mft1, and Thp2), the DEAD box ATPase Sub2, and Yra1. Here we present a 3.7 Å cryo-EM structure of the yeast THO•Sub2 complex. The structure reveals the intimate assembly of THO revolving around its largest subunit Tho2. THO stabilizes a semi-open conformation of the Sub2 ATPase via interactions with Tho2. We show that THO interacts with the SR-like protein Gbp2 through both the N-terminal domain and RRM domains of Gbp2. Crosslinking mass spectrometry analysis supports the extensive interactions between THO and Gbp2, further revealing that RRM domains of Gbp2 are in close proximity to the C-terminal domain of Tho2. We propose that THO serves as a landing pad to configure Gbp2 to facilitate its loading onto mRNP.

Introduction:

Eukaryotic RNA transcription is carried out in the nucleus by the RNA polymerases. During an early stage of mRNA transcription, a 5' cap is added to the newly synthesized mRNA, which is followed by splicing, 3'-end processing and polyadenylation. Nuclear mRNA biogenesis culminates in their export through the nuclear pore complex to the cytoplasm. Many protein factors including serine-arginine (SR) proteins associate with mRNAs to form mature mRNPs for export (Metkar et al., 2018; Singh et al., 2012). The evolutionarily conserved TRanscript-EXport (TREX) complex plays key roles in the highly coordinated mRNP assembly and export (Carmody & Wente, 2009; Chavez et al., 2000; Luo et al., 2001; Strasser & Hurt, 2001; Strasser et al., 2002; Viphakone et al., 2019; Xie & Ren, 2019; Zhou et al., 2000). TREX is recruited to actively transcribed genes (Cheng et al., 2006; Masuda et al., 2005; Strasser et al., 2002) and impacts transcription especially during elongation (Dominguez-Sanchez et al., 2011; Y. Zhang et al., 2016).

The C-terminal domain of the largest subunit of RNA Pol II is highly phosphorylated on the heptapeptide repeats (YSPTSPS) at the Serine 2 position during the elongation phase of the transcription cycle (Hsin & Manley, 2012). Serine 2 phosphorylation coordinates loading of co-transcriptional 3' end processing factors to the transcription machinery (Ahn et al., 2004). In yeast, the primary RNA Pol II CTD Ser2 kinase is the CTDK-1 complex (Cho et al., 2001; Sterner et al., 1995; Wood & Shilatifard, 2006). Growing evidence links the function of TREX and transcriptional CDKs. The yeast TREX component Mft1 interacts genetically with CTDK-1 (Hurt et al., 2004). In addition to their roles during transcription elongation, TREX and CTDK-1 both influence mRNA 3'-end processing and

polyadenylation (Ahn et al., 2004; Rougemaille et al., 2008; Saguez et al., 2008). In humans, the transcriptional kinases are more divergent, at least CDK11, CDK12, and CDK13 are shown to phosphorylate Ser2 on Pol II CTD, all of which have been recognized as tumor suppressors (Cao et al., 2014; Parua & Fisher, 2020). TREX and CDK11 have been shown to interact in human cells and play roles in regulating HIV mRNA 3' end Processing (Pak et al., 2015).

The coordination of TREX and CTDK-1 is largely unknown. Several lines of evidence suggest that a group of shuttling SR proteins could serve as the link for THO and CTDK-1. SR proteins are well recognized as splicing factors, but they also play important roles in coordinating transcription and mRNA export (Reed & Cheng, 2005). In yeast, there are three shuttling SR proteins, Gbp2, Hrb1, and Npl3, which play roles in mRNA export by interacting with the mRNA export receptor Mex67•Mtr2 (Hackmann et al., 2014). In humans, three SR proteins, SRSF1, SRSF3, SRSF7 also shuttle between the nucleus and the cytoplasm to facilitate mRNA export by serving as adaptors for the human ortholog of Mex67•Mtr2, the NXF1•NXT1 complex (Huang et al., 2003; Huang & Steitz, 2005; Muller-McNicoll et al., 2016).

In yeast cells, TAP-tagged Gbp2 and Hrb1 were shown to associate with the CTDK-1 complex (Hurt et al., 2004). Consistent with this observation, using purified recombinant proteins, we recently showed that Gbp2 RRM domains are sufficient to interact with CTDK-1, involving the N-terminal RS domain in its Ctk1 kinase subunit (Xie et al., 2020). We also found that there is a synthetic growth defect when both CTK1 and GBP2 are

knocked out in yeast. The physical and functional interactions between Gbp2 and CTDK-1 provide a link between Gbp2 function and the transcription machinery. Interestingly, in humans, CDK11 directly interacts with SRSF7 (Hu et al., 2003), and together with TREX, all are implicated in HIV-1 mRNA 3' end processing (Pak et al., 2015; Valente et al., 2009). Among the three yeast shuttling SR-like proteins, Gbp2 and Hrb1, but not Npl3 have been shown to rely on the THO components Hpr1 and Mft1 to load onto mRNPs (Hacker & Krebber, 2004). The different requirements could stem from an interaction between THO and Gbp2 and Hrb1, but not Npl3 (Hurt et al., 2004; Martinez-Lumbreras et al., 2016).

Despite extensive studies, how TREX, SR proteins, and CTDK-1 coordinately function during mRNA biogenesis is still not clear. To elucidate the molecular mechanisms, we conducted biochemical and structural studies on the yeast TREX complex and Gbp2. Yeast TREX is a ~470 kDa protein complex comprised of the pentameric THO sub-complex (Tho2, Hpr1, Tex1, Mft1, and Thp2), the DEAD box ATPase Sub2, and Yra1. Thus far structural understanding of the TREX complex has been limited to low resolution structures (Pena et al., 2012; Ren et al., 2017). Here we present a 3.7 Å cryo-EM structure of the yeast THO•Sub2 complex to reveal the molecular details of the THO complex assembly and the THO-Sub2 interactions. We demonstrate direct binding between THO and Gbp2 using recombinant proteins and dissect their mode of interaction using *in vitro* binding studies and crosslinking mass spectrometry (XL-MS) analysis of the THO-Gbp2 complex. Together, we propose that TREX serves as a landing pad to configure the multi-domain Gbp2 and facilitate its loading onto the mRNP.

Results and Discussion

THO directly interacts with the SR-like protein Gbp2

We began by testing the interaction between the THO complex and Gbp2 using purified recombinant proteins. The ~400 kDa THO complex consisting of full-length Tho2, Hpr1, Tex1, Mft1, and Thp2 subunits (denoted by THO-FL, Figure 1A) was expressed in insect cells. Full-length Gbp2 was expressed in insect cells with an N-terminal GST-tag. Using GST pull down assays, we show that Gbp2 directly interacts with THO-FL (Figure 1B). We next tested the binding of Gbp2 to a THO core complex (denoted by THO*, Figure 1A) that contains the ordered regions of all THO's five subunits. We found that THO* is capable of binding to Gbp2, but with reduced interaction compared to THO-FL (Figure 1B). These results suggest that multiple regions in THO are involved in Gbp2 recognition, including both the THO core and the potentially flexible regions that are truncated in THO*.

We next attempted to dissect the domains in Gbp2 that are involved in THO interaction. Gbp2 contains an N-terminal RS domain (NTE) followed by three tandem RRM domains, RRM1, RRM2, and RRM3 (Figure 1A). RRM1 and RRM2 domains are capable of binding to RNA. RRM3 was shown to recognize THO (Martinez-Lumbreras et al., 2016). Interestingly, we found that Gbp2 without RRM3 still binds to THO (Figure 1C). On the other hand, deletion of the N-terminal RS domain of Gbp2 substantially reduced THO interaction, suggesting that the Gbp2 RS domain is required for stable binding to THO.

Together, our binding studies indicate that THO-Gbp2 interaction involves multiple domains from both THO and Gbp2. To provide insights into the underlying molecular

mechanisms of the THO-Gbp2 recognition, we take an integrative approach combining cryo-EM structure determination of the THO* core complex and XL-MS analysis of the THO-FL interaction with Gbp2.

Cryo-EM structure of the THO*•Sub2 complex at 3.7 Å resolution

The THO complex is an integrated structural and functional unit that regulates the activity of Sub2. We previously determined a THO•Sub2 crystal structure at 6.0 Å resolution (Ren et al., 2017). Here, we carried out single particle cryo-EM studies on THO*•Sub2. For cryo-EM sample preparation, the THO*•Sub2 complex was subjected to crosslinking with glutaraldehyde to obtain a more homogeneous sample. We found that THO*•Sub2 forms a higher ordered assembly composed of four THO*•Sub2 protomers (Figure 2-figure supplement 1). This tetrameric assembly has a two-fold symmetry, and it correlates with the asymmetric unit content in our previously determined THO•Sub2 crystal structure. Two of the four THO*•Sub2 protomers are well ordered, whereas the peripheral two protomers are significantly more flexible. We observed an “arch” and a “bridge” that connect a “rigid” THO*•Sub2 protomer and a “mobile” protomer (Figure 2-figure supplement 1D). Our observations suggest that these two protomers are likely components of the functional assembly observed in THO complex isolated from yeast cells (Pena et al., 2012), which is also consistent with the recently published THO•Sub2 structure (Schuller et al., 2020). Details of these features at the THO-THO dimer interface will be discussed in the later section of our XL-MS studies. For obtaining the best quality map for model building, the THO*•Sub2 protomer was extracted from the most ordered two copies and refined to an overall resolution at 3.7 Å (Figure 2-figure supplement 1).

The electron density map allows us to build an atomic model of the THO complex de novo (Figure 2A and Figure 2-figure supplement 2). The THO model contains two thousand residues with 90% assigned residue register. Sub2 was modeled using our previously determined crystal structure (Ren et al., 2017). By having the resolution to build an atomic model, we now reveal the molecular details of the structural core of THO and its interaction with Sub2.

The structure of the THO complex reveals intimate folding of the five subunits (Figure 2B and Figure 2-figure supplement 3). Tho2, the largest subunit spanning the entire length of the elongated THO, plays a critical role in THO assembly. Tho2 can be dissected as "head", "neck", and "trunk" sections. The Tho2 "head" contains an N-terminal helical bundle that clusters with the N-termini of Hpr1, Mft1, and Thp2. Tho2 "neck" is comprised of a helix followed by a loop. The "neck" is embraced by a bi-lobed Hpr1 (lobe A and lobe B). Tho2 "trunk" folds into an alpha solenoid structure, which binds the Tex1 β-propeller at its center and stabilizes a semi-open Sub2 ATPase at its C-terminal end. An extended region at Hpr1 C-terminal region forms a "belt" lining the Tho2 "trunk".

Assembly of the THO•Sub2 complex

Tho2 is the main scaffold upon which other THO constituents assemble. Tho2 features a total contact area of ~9000 $Å^2$ with the other four THO subunits. Tho2 "head" domain binds to a four helix bundle, formed by two pairs of anti-parallel helices contributed by Mft1 and Thp2, respectively (Figure 3A). Tho2 "head" and the helix in its "neck" sandwich the very N-terminal helix of Mft1 (residues 6-17). The opposite side of the Mft1/Thp2 four

171 helix bundle runs in parallel with Hpr1 lobe A (residues 1-230). The Tho2 “neck”,
172 particularly the loop (residues 167-179), is embraced by the Hpr1 lobe A and lobe B
173 (residues 250-490) (Figure 3B). Although the “neck” is largely buried, it contains multiple
174 hydrophilic residues including K171, N173 and E177. Tho2 and Hpr1 residues at this
175 interface are highly conserved from yeast to human (Figure 2-figure supplement 3).
176
177 The “trunk” of Tho2 (residues 180 to 1200) forms an alpha-solenoid. Hpr1 “belt” contains
178 residue assignment from residues 491 to 535 (Figure 3C). It starts from the beginning of
179 the Tho2 “trunk”, featuring aromatic residues at the interface including F511, F515, F518,
180 and W532, and likely extends further to the C-terminus of Tho2 “trunk” as evidenced by
181 our XL-MS studies discussed later. The seven-bladed Tex1 β-propeller sits at the center
182 of the Tho2 “trunk” via blade 4 and 5 (Figure 3D). The loops connecting blade 4/5 (4D5A)
183 and 5/6 (5D6A), as well as the 5BC loop within blade 5 contact a pair of Tho2 helices
184 (residues 626-666), whose opposite side binds to the C-terminal RecA domain of Sub2
185 (Sub2-C). This Tho2-Tex1 interaction is conserved from yeast to human based on the
186 sequence homology (Figure 2-figure supplement 3). In addition, a prominent extension
187 from Tho2 is projected outward perpendicular to the Tho2 “trunk”. The C-terminal part of
188 this extension (residues 464-485) forms a hairpin that winds through the bottom face of
189 the Tex1 β-propeller. This additional Tho2-Tex1 binding mode is likely a yeast specific
190 mechanism as human and other metazoan THOs lack this extension (Figure 2-figure
191 supplement 3).
192

Regulation of the enzymatic activity of the DEAD-box ATPase is vital to the stepwise remodeling reactions mediated by the TREX complex (Xie & Ren, 2019). We previously showed that THO stimulates the ATPase activity of Sub2 (Ren et al., 2017). The cryo-EM structure provides new insights into the molecular details of their interaction. Overall, THO stabilizes a semi-open conformation of Sub2 by interacting with both RecA domains (Sub2-N and Sub2-C). Comparison of the cryo-EM structure and our previous THO•Sub2 crystal structure shows that these two structures are in excellent agreement (Figure 3-figure supplement 1). The cryo-EM structure reveals the atomic details of the THO-Sub2 interactions at the Sub2-C interface (Figure 3E). Sub2-C makes contacts with two pairs of Tho2 helices (residues 625-695). The Sub2 loop consisting of residues 304-308 is situated at the center of the interface featuring electrostatic interactions via E305 and N307. In addition, another Sub2 loop consisting of residues 355-358 makes critical contacts via F355 and R358. The importance of this loop is evidenced by our previous mutagenesis studies that show the ATPase activity of Sub2 mutant E356A/K357A/R358A cannot be activated by THO (Ren et al., 2017). This Sub2 activation mechanism is a conserved mechanism shared by several other DEAD-box proteins including Dbp5 which functions at the terminal step of nuclear mRNA export at the cytoplasmic side of the nuclear pore complex (Folkmann et al., 2011; Mathys et al., 2014; Montpetit et al., 2011; Schutz et al., 2008).

XL-MS analysis of the THO•Gbp2 complex

The THO complex contains a significant amount of potentially flexible regions including ~400 residues at the Tho2 C-terminal end and ~150 residues at the Hpr1 C-terminal end.

These flexible regions are presumably not suitable for structural studies. Our binding studies show that these flexible regions are involved in Gbp2 recognition (Figure 1B). To gain further insights into the THO complex arrangement and the THO-Gbp2 interaction, we took a XL-MS approach (Chait et al., 2016; Leitner et al., 2016; Yu & Huang, 2018) to analyze the complex between THO-FL and Gbp2. We used both EDC and DSS, a carboxyl and amine-reactive crosslinker and an amine specific crosslinker that crosslink residues with Cα-Cα distance less than 17 Å and 30 Å, respectively (Kim et al., 2018; Shi et al., 2014). We obtained a total of 200 unique EDC crosslinks, of which 69 were interprotein crosslinks including 9 crosslinks between Tho2 and Gbp2. We also obtained a total of 133 unique DSS crosslinks to complement the EDC crosslink data, with 53 of these crosslinks being interprotein crosslinks. (Figure 4A, Figure 4A-figure supplement 1, and Table 2). The crosslinking data is highly consistent with the THO structure (Figure 4-figure supplement 1B and 1C). 91% and 100% of the EDC and DSS crosslinks that can be mapped to the structure fall within the expected distance restraint.

Crosslinks between THO subunits provide insights into the C-terminal domain of THO (Tho2-CTD, residues 1200-1597) downstream of the “trunk” domain and the role it plays on the arrangement of the THO-THO dimer. The Tho2-CTD contains a “bridge” that connects THO to the neighboring THO molecule as indicated by our cryo-EM density map (Figure 4B, Figure 2-figure supplement 1). Comparison with the recently published THO-Sub2 structure reveals that the bridge starts at Tho2 residue 1200 (Schuller et al., 2020). The “bridge” is followed by a structured segment, as suggested by the clustered crosslinking between Tho2 (residues 1260 to 1369) and the Hpr1 lobe B (E297, D434,

K462, and K467) as well as Mft1 D129 (Figure 4B). In line with our observation, Tho2 (residues 1279-1405) was shown to form a rigid core through proteolysis and it folds into a helical structure as indicated by CD spectra (Pena et al., 2012). Importantly, crosslinking involving the structured segment indicates that the Tho2-CTD crosses over to the neighboring THO near its Hpr1 lobe B. The structured segment is followed by a highly flexible tail (residues ~1400-1597), as this region crosslinks to spatially separated residues. For example, Tho2 K1576 crosslinks to both Hpr1 lobe B (E297 and D434) and Tex1 (D341). In support of the flexibility of the Tho2 tail, a previous study showed that Tho2 (1411-1530) was highly sensitive to trypsin digestion (Pena et al., 2012). Our XL-MS data further supports the observed THO-THO dimer interface at the “arch”, which is composed of Mft1 and Thp2 from two THO molecules (Schuller et al., 2020). We identified multiple crosslinks involving the “bulge” (Mft1, residues 142-196) including Mft1-K182/Tho2-K1103, Mft1-K165/Tho2-K967, Mft1-K170/Tho2-K967, and Mft1-K174/Tho2-K967 (Figure 2-figure supplement 1D and Table 2). Structural comparison of our cryo-EM structure and the recently published structure reveals significant flexibility in the relative orientation between two THO molecules (Figure 4-figure supplement 2) (Schuller et al., 2020). Of note, as the dimerization of THO is asymmetric, the “bridge” is only observed at the proximal side of the THO dimer. It is conceivable that the Tho2-CTD will exhibit more significant flexibility at the distal side of the THO dimer. Our data also provide insights into the arrangement of the Tex1 C-terminal tail (residues 367-422) and Hpr1-CTD (residues 600-752) (Figure 4-figure supplement 2). The extensive crosslinks observed between Tho2-CTD and Hpr1-CTD suggests that they are spatially close to each other and are likely localized in between two THO molecules. Together, XL-MS

262 results provide critical insights into the regions in THO that are not visible in the cryo-EM
263 structures.
264
265 Crosslinking between Tho2 and Gbp2 indicates that Tho2-CTD is in close proximity to all
266 three Gbp2 RRM domains (Figure 4A and 4C). Each of the three RRM domains crosslinks
267 to the structured segment in Tho2-CTD: RRM1-K190 to Tho2-K1349, RRM2-E241 to
268 Tho2-K1250, and RRM3-D367 to Tho2-K1335. These results suggest that Gbp2 is
269 localized in between two THO molecules near Hpr1 lobe B, as these involved Tho2
270 residues (K1250 and K1335) are crosslinked to Hpr1 lobe B (Figure 4B). Our data also
271 show that each RRM domain crosslinks to the highly flexible tail in Tho2-CTD. It is
272 possible that, in the presence of Gbp2, the Tho2 tail may assume a more specific
273 conformation.
274
275 Our XL-MS results (Figure 4C), together with the *in vitro* binding studies (Figure 1B and
276 1C), demonstrate that Tho2-CTD contributes to Gbp2 interaction. The C-terminal domain
277 of Tho2 also binds to RNA/DNA (Pena, 2012). The function of Tho2-CTD *in vivo* was
278 supported by the growth defect of *tho2-ΔCTD* yeast strains (Pena et al., 2012).
279 Importantly, the synthetic growth defect of *tho2-ΔCTD* and *Δgbp2* strains highlights their
280 functional links (Martinez-Lumbreras et al., 2016).
281
282 As both Gbp2 and Sub2 bind to the C-terminal region of Tho2, we next asked whether
283 Gbp2 and Sub2 can associate with the THO complex together. GST-Gbp2 was used to
284 pull down THO in the presence of Sub2. We found that GST-Gbp2 is able to pull down

both THO and Sub2 (Figure 4D). In addition, THO and Sub2 appear to be in a stoichiometric amount relative to each other. Our results suggest that THO, Sub2, and Gbp2 can form a THO•Sub2•Gbp2 complex, and therefore Gbp2 could function together with the TREX complex during nuclear mRNP maturation.

Working model for coordinated function of TREX and Gbp2

Together with our recent characterization of Gbp2 interaction with the RNA Pol II Ser2 kinase CTDK-1 complex, we propose a working model for the coordinated function between TREX, Gbp2, and CTDK-1 (Figure 5). Gbp2 interaction with CTDK-1 provides a means to associate with the transcription machinery (Hurt et al., 2004; Xie et al., 2020). We envision that TREX and Gbp2 function coordinately during nuclear mRNP maturation and surveillance. During transcription, faulty assembly of mRNPs is a threat to genomic stability. If the defective mRNPs persist, they need to be sensed by a surveillance system and degraded. In yeast, Gbp2 and Hrb1 were shown to play key roles in mRNP surveillance (Hackmann et al., 2014). Interactions between Gbp2 and Mex67 for export and between Gbp2 and Mtr4 for degradation through the RNA exosome complex are mutually exclusive. TREX travels with the transcription machinery (Meinel et al., 2013) and its function in mRNP assembly is well documented. In THO/Sub2 mutant yeast cells, mRNP assembly is defective and faulty mRNPs cannot be degraded efficiently, which leads to the formation of heavy chromatin (Rougemaille et al., 2008; Saguez et al., 2008). In humans, depletion of TREX complex components leads to R-loop accumulation, transcriptional elongation defects, and trapped mRNP in nuclear speckles. (Dias et al., 2010; Dominguez-Sanchez et al., 2011; Perez-Calero et al., 2020; Wang et al., 2018).

The extensive interactions between THO and Gbp2 suggest that THO could serve as a landing pad for Gbp2 loading onto mRNPs to function as a key surveillance factor during mRNP maturation. Interestingly, in human cells, TREX was shown to interact with multiple domains of the mRNP export receptor NXF1•NXT1 to facilitate its loading onto mRNPs (Viphakone et al., 2019). Given that Gbp2 interacts with the yeast export receptor Mex67•Mtr2 (Hackmann, 2014), the interplay between TREX, Gbp2, and Mex67•Mtr2 during mRNP biogenesis warrants further study.

Methods

Plasmids and proteins

Both THO-FL and the THO* core complex were expressed in High-Five insect cells by coinfection of recombinant baculoviruses. THO-FL contains full length *S. cerevisiae* Tho2 (residues 1-1597), Hpr1 (residues 1-752), Tex1 (residues 1-422), Mft1 (residues 1-392), and Thp2 (residues 1-261) subunits and the former four subunits each contains a TEV cleavable N-terminal His tag. The THO* complex contains *S. cerevisiae* Tho2 (residues 1-1257), Hpr1 (residues 1-603), Mft1 (residues 1-256), full length Thp2, and *S. bayanas* Tex1 (residues 1-380) with Tho2 and Hpr1 each containing a TEV cleavable N-terminal His tag. High-Five cells were harvested 48 hr after infection. The cells were sonicated in a lysis buffer containing 50 mM Tris pH 8.0, 300 mM NaCl, 10 mM imidazole, 1 mM PMSF, 5 mg/L aprotinin, 1 mg/L pepstatin, 1 mg/L leupeptin, and 0.5 mM TCEP. THO complexes were purified by Ni affinity chromatography, followed by TEV digestion to remove His tags. The proteins were then purified on a mono Q column (GE Healthcare) and subjected to further size exclusion purification with a Superose 6 column (GE Healthcare) in 10 mM Tris pH 8.0, 150 mM NaCl, and 0.5 mM TCEP.

GST tagged Gbp2 (residues 1-427) and Gbp2ΔRRM3 (residues 1-316) were expressed in High-Five cells. Cells were lysed in the same condition as the THO complexes. The GST tagged Gbp2 proteins were purified using glutathione sepharose 4B resin (GE Healthcare) followed by size exclusion chromatography using a Superdex 200 column (GE Healthcare) in 10 mM Tris pH 8.0, 300 mM NaCl, and 0.5 mM TCEP.

Sub2 and Gbp2ΔN (residues 107-427) were expressed in Rosetta *E. coli* cells (Stratagene) with an N-terminal TEV cleavable GST tag. Protein expression was induced at an OD_{600} of 1.0 with 0.5 mM IPTG at 20 °C for 16 hrs. Cells were lysed in the same lysis buffer as mentioned above. Proteins were first purified using glutathione sepharose 4B resin. For Sub2, the GST tag was removed by TEV, and the protein was purified on a mono Q column. Untagged Sub2 and GST-Gbp2ΔN were further purified on a Superdex 200 column in 10 mM Tris pH 8.0, 150 mM NaCl, and 0.5 mM TCEP.

All purified proteins were concentrated, flash frozen in liquid nitrogen, and stored at -80°C.

Cryo-EM Sample preparation and data collection

Purified THO* and Sub2 were first buffer exchanged to 10 mM HEPES pH 7.0, 100 mM potassium acetate, and 0.5 mM TCEP. THO* was incubated with 3-fold molar excess of Sub2 in the presence of 0.05% glutaraldehyde for 30 min at RT. Crosslinking was quenched with 0.1 M Tris pH 8.0 and the sample was concentrated to 0.5 mg/mL. 1.5 µl of THO*•Sub2 was applied to a glow-discharged UltrAuFoil R 1.2/1.3 grids (Quantifoil). Grids were blotted for 3 s with a blotting force of 3 and 100% humidity at 22 °C and plunged into liquid ethane using an FEI Vitrobot Mark IV (Thermo Fisher).

Electron micrographs were acquired with a Titan Krios electron microscope (Thermo Fisher) equipped with a Falcon 3 detector (Thermo Fisher). Movies were collected with EPU with a calibrated pixel size of 0.681 Å/pixel. A total of 4907 movies were collected

with a defocus range from 0.8 μm to 2.0 μm. Description of the cryo-EM data collection parameters can be found in Table 1.

Cryo-EM data processing

Motion correction was performed using MotionCor2 (Zheng et al., 2017). The parameters of the contrast transfer function (CTF) were estimated using Gctf (K. Zhang, 2016). We initially selected 396 K particles from 4907 micrographs with automatic particle picking in RELION-3 (Zivanov et al., 2018). The picked particles were binned by 2 and subjected to reference-free 2D classification. 205 K particles were selected for 3D classification with C2 symmetry using an initial model generated by EMAN2 (Tang et al., 2007). Each particle contains four copies of the THO•Sub2 complex with two copies significantly more flexible than the others. 15 K particles were selected for 3D refinement using a mask covering the two ordered THO•Sub2 molecules with C2 symmetry. The particles were then re-extracted at the original pixel size of 0.681 Å/pixel and subjected to Bayesian polishing, CTF refinement, and 3D refinement. Refinement of the entire four copies of THO•Sub2 molecules generated a map at 4.80 Å resolution. We extracted 30 K THO•Sub2 protomers from the ordered two copies and refinement using a mask covering one THO•Sub2 molecule yielded a map of THO•Sub2 at 3.70 Å resolution with a sharpening B factor of 86 $Å^2$ as assessed by an FSC threshold of 0.143.

Model building

The 3.70 Å THO•Sub2 map was used for model building in COOT (Emsley et al., 2010). The five subunit THO complex was built de novo. Individual RecA domains of Sub2 were

placed using our previously determined atomic resolution structure (PDB ID 5SUP). The THO•Sub2 model was subjected to real-space refinement in Phenix (Adams et al., 2010). The final THO•Sub2 model contains Tho2 (residues 37 to 913, followed by 10 poly-Ala helices at the C-terminus), Hpr1 (residues 4 to 535), Tex1 (residues 68 to 366), Mft1 (residues 5 to 227), Thp2 (residues 8 to 227), and Sub2. Figures were prepared using Chimera (Pettersen et al., 2004) or PyMOL (Molecular Graphics System, Schrodinger, LLC).

GST pull-down assays

1 μM of GST or GST-tagged Gbp2 variants was incubated with 1 μM of THO variants or with 1 μM of THO and 2 μM of Sub2 as indicated in the binding buffer (20 mM HEPES pH 7.0, 80 mM NaCl, and 0.5 mM TCEP) at room temperature for 10 min. The reaction mixtures were then added to ~15 μL glutathione resin in an Eppendorf tube and binding was allowed to proceed at room temperature for 30 min with gentle tapping to mix every 3-5 min. Beads were washed twice with 500 μL washing buffer containing 20 mM HEPES pH 7.0, 80 mM NaCl (for Figure 1B) or 50 mM NaCl (for Figure 1C and Figure 4D), and 0.5 mM TCEP. Bound proteins were eluted with washing buffer supplemented with 20 mM glutathione and analyzed using Coomassie-stained SDS-PAGE gels. The experiments were repeated three times independently.

Crosslinking mass spectrometry analysis

For EDC crosslinking, 1 μM of THO-FL and 1 μM of GST-Gbp2 were incubated at 10 mM HEPES pH 7.0, 105 mM NaCl, 0.5 mM TCEP in the presence of 20 mM EDC and 0.5 mM

sulfo-DHS at room temperature for 40 min. The reaction was quenched at room temperature for 20 min by adding Tris pH 8.0 and β-mercaptoethanol to a final concentration of 50 mM and 20 mM, respectively. DSS crosslinking was performed in the same conditions except that 0.5 mM DSS was used and only Tris pH 8.0 was used for quenching the reaction.

The DSS and EDC cross-linked samples were directly processed for in-solution Trypsin and Lys-C digestion. The samples were reduced with 5 mM DTT and 5 mM TCEP in 8M urea buffer (50 mM Ammonium bicarbonate), and were then incubated with 30mM iodoacetamide at room temperature for 30 minutes in the dark. 30-45 µg of the purified complex was digested with Trypsin and Lys-C using a 1:100 ratio for each protease upon diluting the sample to 1 M urea. The proteolysis reaction occurred overnight (12-16 hours) at 37°C. After overnight digestion with trypsin, the complex was digested with an additional 1:100 ratio of trypsin at 37°C for 2 hours. The resulting mixture was acidified, desalted by using a C18 cartridge (Sep-Pak, Waters).

1-2 µg of the trypsin digested crosslinked complex was analyzed with a nano-LC 1200 that is coupled online with a Q Exactive™ HF-X Hybrid Quadrupole Orbitrap™ mass spectrometer (Thermo Fisher) (Xiang, Nambulli, et al., 2020; Xiang, Shen, et al., 2020). Briefly, desalted peptides were loaded onto a Picochip column (C18, 1.9 µm particle size, 200 Å pore size, 50 µm × 25 cm; New Objective) and eluted using a 60-min liquid chromatography gradient (5% B–8% B, 0–2 min; 8% B–40% B, 2-50 min; 40%B–100% B, 50-60 min; mobile phase A consisted of 0.1% formic acid (FA), and mobile phase B

consisted of 0.1% FA in 80% acetonitrile). The flow rate was ~350 nl/min. The QE HF-X instrument was operated in the data-dependent mode, where the top 6 most abundant ions (mass range 350 – 2,000, charge state 4 - 8) were fragmented by high-energy collisional dissociation (HCD). The target resolution was 120,000 for MS and 15,000 for tandem MS (MS/MS) analyses. The quadrupole isolation window was 1.6 Th, and the maximum injection time for MS/MS was set at 300 ms.

After the MS analysis, the data was searched by pLink2 for the identification of cross-linked peptides (Chen et al., 2019). The mass accuracy was specified as 10 and 20 p.p.m. for MS and MS/MS, respectively. Other search parameters included cysteine carbamidomethylation as a fixed modification and methionine oxidation as a variable modification. A maximum of three trypsin missed-cleavage sites were allowed. The crosslink spectra were then manually checked to remove potential false-positive identifications as previously described (Xiang, Shen, et al., 2020). The crosslinking data was analyzed by CX-Circos (http://cx-circos.net). The distance distribution of the crosslinks onto the THO structure was performed with Xlink Analyzer (Kosinski et al., 2015).

Acknowledgments

We thank Scott Collier and Melissa Chambers at the Center for Structural Biology Cryo-EM Facility at Vanderbilt University for assistance in Cryo-EM data collection. We thank members of the Wente laboratory for discussions. This work was supported by NIGMS grants R35 GM133743 to Y.R. and GM137905 to Y.S., and funds from Vanderbilt University School of Medicine to Y.R.. BPC is supported by NIH/NCI training grant T32CA119925.

Data availability

The cryo-EM density maps will be deposited in the Electron Microscopy Data Bank. The coordinates of the THO•Sub2 complex will be deposited in the Protein Data Bank.

Competing interests

The authors declare no competing interests.

References

Adams, P. D., Afonine, P. V., Bunkoczi, G., Chen, V. B., Davis, I. W., Echols, N., Headd, J. J., Hung, L. W., Kapral, G. J., Grosse-Kunstleve, R. W., McCoy, A. J., Moriarty, N. W., Oeffner, R., Read, R. J., Richardson, D. C., Richardson, J. S., Terwilliger, T. C., & Zwart, P. H. (2010). PHENIX: a comprehensive Python-based system for macromolecular structure solution. *Acta Crystallogr D Biol Crystallogr, 66*(Pt 2), 213-221. doi:10.1107/S0907444909052925

Ahn, S. H., Kim, M., & Buratowski, S. (2004). Phosphorylation of serine 2 within the RNA polymerase II C-terminal domain couples transcription and 3' end processing. *Mol Cell, 13*(1), 67-76. doi:10.1016/s1097-2765(03)00492-1

Cao, L., Chen, F., Yang, X., Xu, W., Xie, J., & Yu, L. (2014). Phylogenetic analysis of CDK and cyclin proteins in premetazoan lineages. *BMC Evol Biol, 14*, 10. doi:10.1186/1471-2148-14-10

Carmody, S. R., & Wente, S. R. (2009). mRNA nuclear export at a glance. *J Cell Sci, 122*(Pt 12), 1933-1937. doi:10.1242/jcs.041236

Chait, B. T., Cadene, M., Olinares, P. D., Rout, M. P., & Shi, Y. (2016). Revealing Higher Order Protein Structure Using Mass Spectrometry. *Journal of the American Society for Mass Spectrometry, 27*(6), 952-965. doi:10.1007/s13361-016-1385-1

Chavez, S., Beilharz, T., Rondon, A. G., Erdjument-Bromage, H., Tempst, P., Svejstrup, J. Q., Lithgow, T., & Aguilera, A. (2000). A protein complex containing Tho2, Hpr1, Mft1 and a novel protein, Thp2, connects transcription elongation with mitotic recombination in Saccharomyces cerevisiae. *EMBO J, 19*(21), 5824-5834. doi:10.1093/emboj/19.21.5824

Chen, Z. L., Meng, J. M., Cao, Y., Yin, J. L., Fang, R. Q., Fan, S. B., Liu, C., Zeng, W. F., Ding, Y. H., Tan, D., Wu, L., Zhou, W. J., Chi, H., Sun, R. X., Dong, M. Q., & He, S. M. (2019). A high-speed search engine pLink 2 with systematic evaluation for proteome-scale identification of cross-linked peptides. *Nat Commun, 10*(1), 3404. doi:10.1038/s41467-019-11337-z

Cheng, H., Dufu, K., Lee, C. S., Hsu, J. L., Dias, A., & Reed, R. (2006). Human mRNA export machinery recruited to the 5' end of mRNA. *Cell, 127*(7), 1389-1400. doi:10.1016/j.cell.2006.10.044

Cho, E. J., Kobor, M. S., Kim, M., Greenblatt, J., & Buratowski, S. (2001). Opposing effects of Ctk1 kinase and Fcp1 phosphatase at Ser 2 of the RNA polymerase II C-terminal domain. *Genes Dev, 15*(24), 3319-3329. doi:10.1101/gad.935901

Dias, A. P., Dufu, K., Lei, H., & Reed, R. (2010). A role for TREX components in the release of spliced mRNA from nuclear speckle domains. *Nat Commun, 1*, 97. doi:10.1038/ncomms1103

Dominguez-Sanchez, M. S., Barroso, S., Gomez-Gonzalez, B., Luna, R., & Aguilera, A. (2011). Genome instability and transcription elongation impairment in human cells depleted of THO/TREX. *PLoS Genet, 7*(12), e1002386. doi:10.1371/journal.pgen.1002386

Emsley, P., Lohkamp, B., Scott, W. G., & Cowtan, K. (2010). Features and development of Coot. *Acta Crystallogr D Biol Crystallogr, 66*(Pt 4), 486-501. doi:10.1107/S0907444910007493

Folkmann, A. W., Noble, K. N., Cole, C. N., & Wente, S. R. (2011). Dbp5, Gle1-IP6 and Nup159: a working model for mRNP export. *Nucleus, 2*(6), 540-548. doi:10.4161/nucl.2.6.17881

Hacker, S., & Krebber, H. (2004). Differential export requirements for shuttling serine/arginine-type mRNA-binding proteins. *J Biol Chem, 279*(7), 5049-5052. doi:10.1074/jbc.C300522200

508 Hackmann, A., Wu, H., Schneider, U. M., Meyer, K., Jung, K., & Krebber, H. (2014). Quality
509 control of spliced mRNAs requires the shuttling SR proteins Gbp2 and Hrb1. *Nat Commun,*
510 *5*, 3123. doi:10.1038/ncomms4123
511 Hsin, J. P., & Manley, J. L. (2012). The RNA polymerase II CTD coordinates transcription and
512 RNA processing. *Genes Dev, 26*(19), 2119-2137. doi:10.1101/gad.200303.112
513 Hu, D., Mayeda, A., Trembley, J. H., Lahti, J. M., & Kidd, V. J. (2003). CDK11 complexes
514 promote pre-mRNA splicing. *J Biol Chem, 278*(10), 8623-8629.
515 doi:10.1074/jbc.M210057200
516 Huang, Y., Gattoni, R., Stevenin, J., & Steitz, J. A. (2003). SR splicing factors serve as adapter
517 proteins for TAP-dependent mRNA export. *Mol Cell, 11*(3), 837-843. doi:10.1016/s1097-
518 2765(03)00089-3
519 Huang, Y., & Steitz, J. A. (2005). SRprises along a messenger's journey. *Mol Cell, 17*(5), 613-615.
520 doi:10.1016/j.molcel.2005.02.020
521 Hurt, E., Luo, M. J., Rother, S., Reed, R., & Strasser, K. (2004). Cotranscriptional recruitment of
522 the serine-arginine-rich (SR)-like proteins Gbp2 and Hrb1 to nascent mRNA via the TREX
523 complex. *Proc Natl Acad Sci U S A, 101*(7), 1858-1862. doi:10.1073/pnas.0308663100
524 Kim, S. J., Fernandez-Martinez, J., Nudelman, I., Shi, Y., Zhang, W. Z., Raveh, B., Herricks, T.,
525 Slaughter, B. D., Hogan, J. A., Upla, P., Chemmama, I. E., Pellarin, R., Echeverria, I.,
526 Shivaraju, M., Chaudhury, A. S., Wang, J. J., Williams, R., Unruh, J. R., Greenberg, C. H.,
527 Jacobs, E. Y., Yu, Z. H., de la Cruz, M. J., Mironska, R., Stokes, D. L., Aitchison, J. D.,
528 Jarrold, M. F., Gerton, J. L., Ludtke, S. J., Akey, C. W., Chait, B. T., Sali, A., & Rout, M.
529 P. (2018). Integrative structure and functional anatomy of a nuclear pore complex. *Nature,*
530 *555*(7697), 475-+. doi:10.1038/nature26003
531 Kosinski, J., von Appen, A., Ori, A., Karius, K., Muller, C. W., & Beck, M. (2015). Xlink Analyzer:
532 software for analysis and visualization of cross-linking data in the context of three-
533 dimensional structures. *J Struct Biol, 189*(3), 177-183. doi:10.1016/j.jsb.2015.01.014
534 Leitner, A., Faini, M., Stengel, F., & Aebersold, R. (2016). Crosslinking and Mass Spectrometry:
535 An Integrated Technology to Understand the Structure and Function of Molecular
536 Machines. *Trends in Biochemical Sciences, 41*(1), 20-32. doi:10.1016/j.tibs.2015.10.008
537 Luo, M. L., Zhou, Z., Magni, K., Christoforides, C., Rappsilber, J., Mann, M., & Reed, R. (2001).
538 Pre-mRNA splicing and mRNA export linked by direct interactions between UAP56 and
539 Aly. *Nature, 413*(6856), 644-647. doi:10.1038/35098106
540 Martinez-Lumbreras, S., Taverniti, V., Zorrilla, S., Seraphin, B., & Perez-Canadillas, J. M. (2016).
541 Gbp2 interacts with THO/TREX through a novel type of RRM domain. *Nucleic Acids Res,*
542 *44*(1), 437-448. doi:10.1093/nar/gkv1303
543 Masuda, S., Das, R., Cheng, H., Hurt, E., Dorman, N., & Reed, R. (2005). Recruitment of the
544 human TREX complex to mRNA during splicing. *Genes Dev, 19*(13), 1512-1517.
545 doi:10.1101/gad.1302205
546 Mathys, H., Basquin, J., Ozgur, S., Czarnocki-Cieciura, M., Bonneau, F., Aartse, A., Dziembowski,
547 A., Nowotny, M., Conti, E., & Filipowicz, W. (2014). Structural and biochemical insights
548 to the role of the CCR4-NOT complex and DDX6 ATPase in microRNA repression. *Mol*
549 *Cell, 54*(5), 751-765. doi:10.1016/j.molcel.2014.03.036
550 Meinel, D. M., Burkert-Kautzsch, C., Kieser, A., O'Duibhir, E., Siebert, M., Mayer, A., Cramer,
551 P., Soding, J., Holstege, F. C., & Strasser, K. (2013). Recruitment of TREX to the
552 transcription machinery by its direct binding to the phospho-CTD of RNA polymerase II.
553 *PLoS Genet, 9*(11), e1003914. doi:10.1371/journal.pgen.1003914

554 Metkar, M., Ozadam, H., Lajoie, B. R., Imakaev, M., Mirny, L. A., Dekker, J., & Moore, M. J.
555 (2018). Higher-Order Organization Principles of Pre-translational mRNPs. *Mol Cell, 72*(4),
556 715-726 e713. doi:10.1016/j.molcel.2018.09.012
557 Montpetit, B., Thomsen, N. D., Helmke, K. J., Seeliger, M. A., Berger, J. M., & Weis, K. (2011).
558 A conserved mechanism of DEAD-box ATPase activation by nucleoporins and InsP6 in
559 mRNA export. *Nature, 472*(7342), 238-242. doi:10.1038/nature09862
560 Muller-McNicoll, M., Botti, V., de Jesus Domingues, A. M., Brandl, H., Schwich, O. D., Steiner,
561 M. C., Curk, T., Poser, I., Zarnack, K., & Neugebauer, K. M. (2016). SR proteins are NXF1
562 adaptors that link alternative RNA processing to mRNA export. *Genes Dev, 30*(5), 553-
563 566. doi:10.1101/gad.276477.115
564 Pak, V., Eifler, T. T., Jager, S., Krogan, N. J., Fujinaga, K., & Peterlin, B. M. (2015). CDK11 in
565 TREX/THOC Regulates HIV mRNA 3' End Processing. *Cell Host Microbe, 18*(5), 560-
566 570. doi:10.1016/j.chom.2015.10.012
567 Parua, P. K., & Fisher, R. P. (2020). Dissecting the Pol II transcription cycle and derailing cancer
568 with CDK inhibitors. *Nat Chem Biol, 16*(7), 716-724. doi:10.1038/s41589-020-0563-4
569 Pena, A., Gewartowski, K., Mroczek, S., Cuellar, J., Szykowska, A., Prokop, A., Czarnocki-
570 Cieciura, M., Piwowarski, J., Tous, C., Aguilera, A., Carrascosa, J. L., Valpuesta, J. M., &
571 Dziembowski, A. (2012). Architecture and nucleic acids recognition mechanism of the
572 THO complex, an mRNP assembly factor. *EMBO J, 31*(6), 1605-1616.
573 doi:10.1038/emboj.2012.10
574 Perez-Calero, C., Bayona-Feliu, A., Xue, X., Barroso, S. I., Munoz, S., Gonzalez-Basallote, V. M.,
575 Sung, P., & Aguilera, A. (2020). UAP56/DDX39B is a major cotranscriptional RNA-DNA
576 helicase that unwinds harmful R loops genome-wide. *Genes Dev, 34*(13-14), 898-912.
577 doi:10.1101/gad.336024.119
578 Pettersen, E. F., Goddard, T. D., Huang, C. C., Couch, G. S., Greenblatt, D. M., Meng, E. C., &
579 Ferrin, T. E. (2004). UCSF Chimera--a visualization system for exploratory research and
580 analysis. *J Comput Chem, 25*(13), 1605-1612. doi:10.1002/jcc.20084
581 Reed, R., & Cheng, H. (2005). TREX, SR proteins and export of mRNA. *Curr Opin Cell Biol,*
582 *17*(3), 269-273. doi:10.1016/j.ceb.2005.04.011
583 Ren, Y., Schmiege, P., & Blobel, G. (2017). Structural and biochemical analyses of the DEAD-
584 box ATPase Sub2 in association with THO or Yra1. *Elife, 6*. doi:10.7554/eLife.20070
585 Rougemaille, M., Dieppois, G., Kisseleva-Romanova, E., Gudipati, R. K., Lemoine, S., Blugeon,
586 C., Boulay, J., Jensen, T. H., Stutz, F., Devaux, F., & Libri, D. (2008). THO/Sub2p
587 functions to coordinate 3'-end processing with gene-nuclear pore association. *Cell, 135*(2),
588 308-321. doi:10.1016/j.cell.2008.08.005
589 Saguez, C., Schmid, M., Olesen, J. R., Ghazy, M. A., Qu, X., Poulsen, M. B., Nasser, T., Moore,
590 C., & Jensen, T. H. (2008). Nuclear mRNA surveillance in THO/sub2 mutants is triggered
591 by inefficient polyadenylation. *Mol Cell, 31*(1), 91-103. doi:10.1016/j.molcel.2008.04.030
592 Schuller, S. K., Schuller, J. M., Prabu, J. R., Baumgartner, M., Bonneau, F., Basquin, J., & Conti,
593 E. (2020). Structural insights into the nucleic acid remodeling mechanisms of the yeast
594 THO-Sub2 complex. *Elife, 9*. doi:10.7554/eLife.61467
595 Schutz, P., Bumann, M., Oberholzer, A. E., Bieniossek, C., Trachsel, H., Altmann, M., & Baumann,
596 U. (2008). Crystal structure of the yeast eIF4A-eIF4G complex: an RNA-helicase
597 controlled by protein-protein interactions. *Proc Natl Acad Sci U S A, 105*(28), 9564-9569.
598 doi:10.1073/pnas.0800418105

599 Shi, Y., Fernandez-Martinez, J., Tjioe, E., Pellarin, R., Kim, S. J., Williams, R., Schneidman-
600 Duhovny, D., Sali, A., Rout, M. P., & Chait, B. T. (2014). Structural characterization by
601 cross-linking reveals the detailed architecture of a coatomer-related heptameric module
602 from the nuclear pore complex. *Mol Cell Proteomics, 13*(11), 2927-2943.
603 doi:10.1074/mcp.M114.041673
604 Singh, G., Kucukural, A., Cenik, C., Leszyk, J. D., Shaffer, S. A., Weng, Z., & Moore, M. J. (2012).
605 The Cellular EJC Interactome Reveals Higher-Order mRNP Structure and an EJC-SR
606 Protein Nexus. *Cell, 151*(4), 915-916. doi:10.1016/j.cell.2012.10.032
607 Sterner, D. E., Lee, J. M., Hardin, S. E., & Greenleaf, A. L. (1995). The yeast carboxyl-terminal
608 repeat domain kinase CTDK-I is a divergent cyclin-cyclin-dependent kinase complex. *Mol*
609 *Cell Biol, 15*(10), 5716-5724. doi:10.1128/mcb.15.10.5716
610 Strasser, K., & Hurt, E. (2001). Splicing factor Sub2p is required for nuclear mRNA export through
611 its interaction with Yra1p. *Nature, 413*(6856), 648-652. doi:10.1038/35098113
612 Strasser, K., Masuda, S., Mason, P., Pfannstiel, J., Oppizzi, M., Rodriguez-Navarro, S., Rondon,
613 A. G., Aguilera, A., Struhl, K., Reed, R., & Hurt, E. (2002). TREX is a conserved complex
614 coupling transcription with messenger RNA export. *Nature, 417*(6886), 304-308.
615 doi:10.1038/nature746
616 Tang, G., Peng, L., Baldwin, P. R., Mann, D. S., Jiang, W., Rees, I., & Ludtke, S. J. (2007).
617 EMAN2: an extensible image processing suite for electron microscopy. *J Struct Biol,*
618 *157*(1), 38-46. doi:10.1016/j.jsb.2006.05.009
619 Valente, S. T., Gilmartin, G. M., Venkatarama, K., Arriagada, G., & Goff, S. P. (2009). HIV-1
620 mRNA 3' end processing is distinctively regulated by eIF3f, CDK11, and splice factor 9G8.
621 *Mol Cell, 36*(2), 279-289. doi:10.1016/j.molcel.2009.10.004
622 Viphakone, N., Sudbery, I., Griffith, L., Heath, C. G., Sims, D., & Wilson, S. A. (2019). Co-
623 transcriptional Loading of RNA Export Factors Shapes the Human Transcriptome. *Mol*
624 *Cell, 75*(2), 310-323 e318. doi:10.1016/j.molcel.2019.04.034
625 Wang, K., Wang, L., Wang, J., Chen, S., Shi, M., & Cheng, H. (2018). Intronless mRNAs transit
626 through nuclear speckles to gain export competence. *J Cell Biol, 217*(11), 3912-3929.
627 doi:10.1083/jcb.201801184
628 Wood, A., & Shilatifard, A. (2006). Bur1/Bur2 and the Ctk complex in yeast: the split personality
629 of mammalian P-TEFb. *Cell Cycle, 5*(10), 1066-1068. doi:10.4161/cc.5.10.2769
630 Xiang, Y., Nambulli, S., Xiao, Z., Liu, H., Sang, Z., Duprex, W. P., Schneidman-Duhovny, D.,
631 Zhang, C., & Shi, Y. (2020). Versatile and multivalent nanobodies efficiently neutralize
632 SARS-CoV-2. *Science*. doi:10.1126/science.abe4747
633 Xiang, Y., Shen, Z., & Shi, Y. (2020). Chemical Cross-Linking and Mass Spectrometric Analysis
634 of the Endogenous Yeast Exosome Complexes. *Methods Mol Biol, 2062*, 383-400.
635 doi:10.1007/978-1-4939-9822-7_18
636 Xie, Y., Lord, C. L., Clarke, B. P., Ivey, A. L., S., Hill P., W., McDonald H., Wente, S. R., & Ren,
637 Y. (2020). Structure and activation mechanism of the yeast RNA Pol II CTD kinase CTDK-
638 1 complex. *Proc Natl Acad Sci U S A (manuscript in press)*.
639 Xie, Y., & Ren, Y. (2019). Mechanisms of nuclear mRNA export: A structural perspective. *Traffic,*
640 *20*(11), 829-840. doi:10.1111/tra.12691
641 Yu, C., & Huang, L. (2018). Cross-Linking Mass Spectrometry: An Emerging Technology for
642 Interactomics and Structural Biology. *Analytical Chemistry, 90*(1), 144-165.
643 doi:10.1021/acs.analchem.7b04431

644 Zhang, K. (2016). Gctf: Real-time CTF determination and correction. *J Struct Biol, 193*(1), 1-12.
645 doi:10.1016/j.jsb.2015.11.003
646 Zhang, Y., French, S. L., Beyer, A. L., & Schneider, D. A. (2016). The Transcription Factor THO
647 Promotes Transcription Initiation and Elongation by RNA Polymerase I. *J Biol Chem,*
648 *291*(6), 3010-3018. doi:10.1074/jbc.M115.673442
649 Zheng, S. Q., Palovcak, E., Armache, J. P., Verba, K. A., Cheng, Y., & Agard, D. A. (2017).
650 MotionCor2: anisotropic correction of beam-induced motion for improved cryo-electron
651 microscopy. *Nat Methods, 14*(4), 331-332. doi:10.1038/nmeth.4193
652 Zhou, Z., Luo, M. J., Straesser, K., Katahira, J., Hurt, E., & Reed, R. (2000). The protein Aly links
653 pre-messenger-RNA splicing to nuclear export in metazoans. *Nature, 407*(6802), 401-405.
654 doi:10.1038/35030160
655 Zivanov, J., Nakane, T., Forsberg, B. O., Kimanius, D., Hagen, W. J., Lindahl, E., & Scheres, S.
656 H. (2018). New tools for automated high-resolution cryo-EM structure determination in
657 RELION-3. *Elife, 7*. doi:10.7554/eLife.42166
658
659

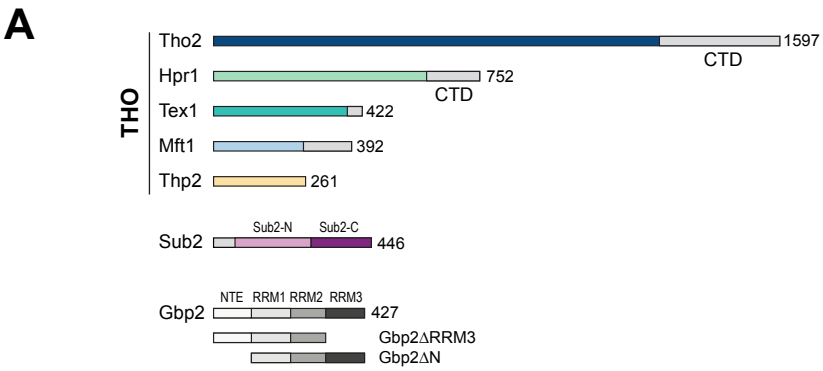

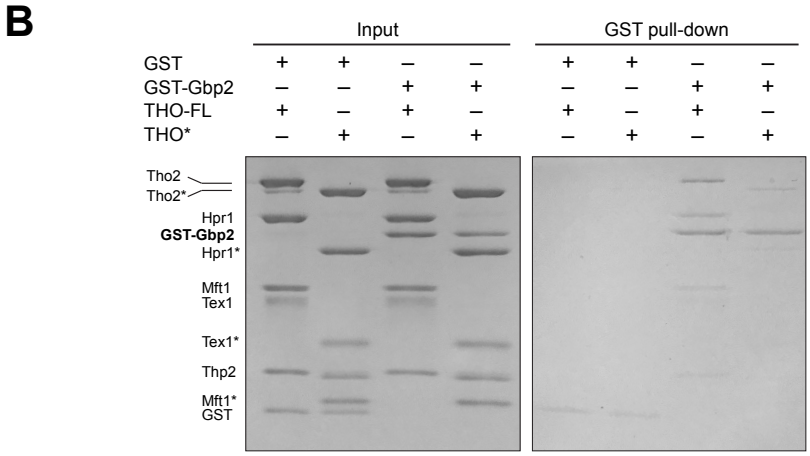

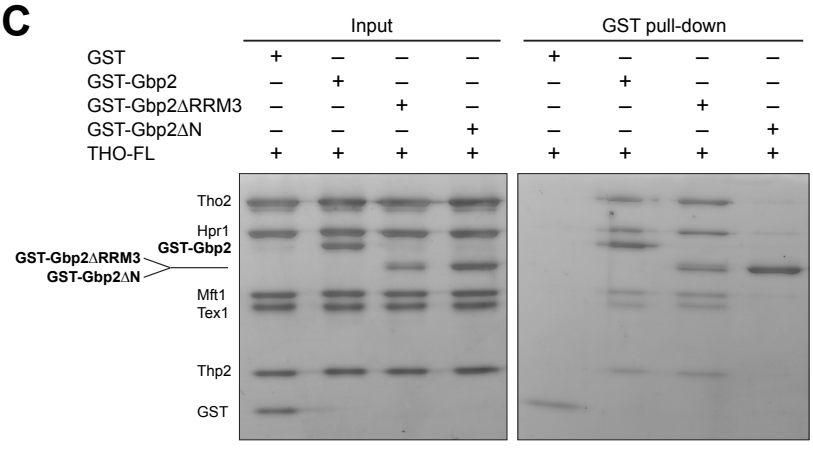

660 **Figure 1. The THO complex directly interacts with the SR-like protein Gbp2. A)**
661 Domain organization of the THO complex, Sub2, and Gbp2. Within THO, the protein
662 regions that are included in the core THO* complex are colored (Tho2 in blue, Hpr1 in
663 green, Tex1 in cyan, Mft1 in light blue, and Thp2 in yellow). Sub2 is colored in pink (Sub2-
664 N) and purple (Sub2-C). Gbp2 contains an N-terminal extension (NTE) followed by three
665 RRM domains. **B)** THO directly interacts with Gbp2. *In vitro* GST-pull down assays with
666 purified recombinant proteins show that both THO-FL and THO* bind to Gbp2 with the
667 former exhibiting stronger interaction. **C)** THO binding to Gpb2 requires the N-terminal
668 extension of Gbp2.

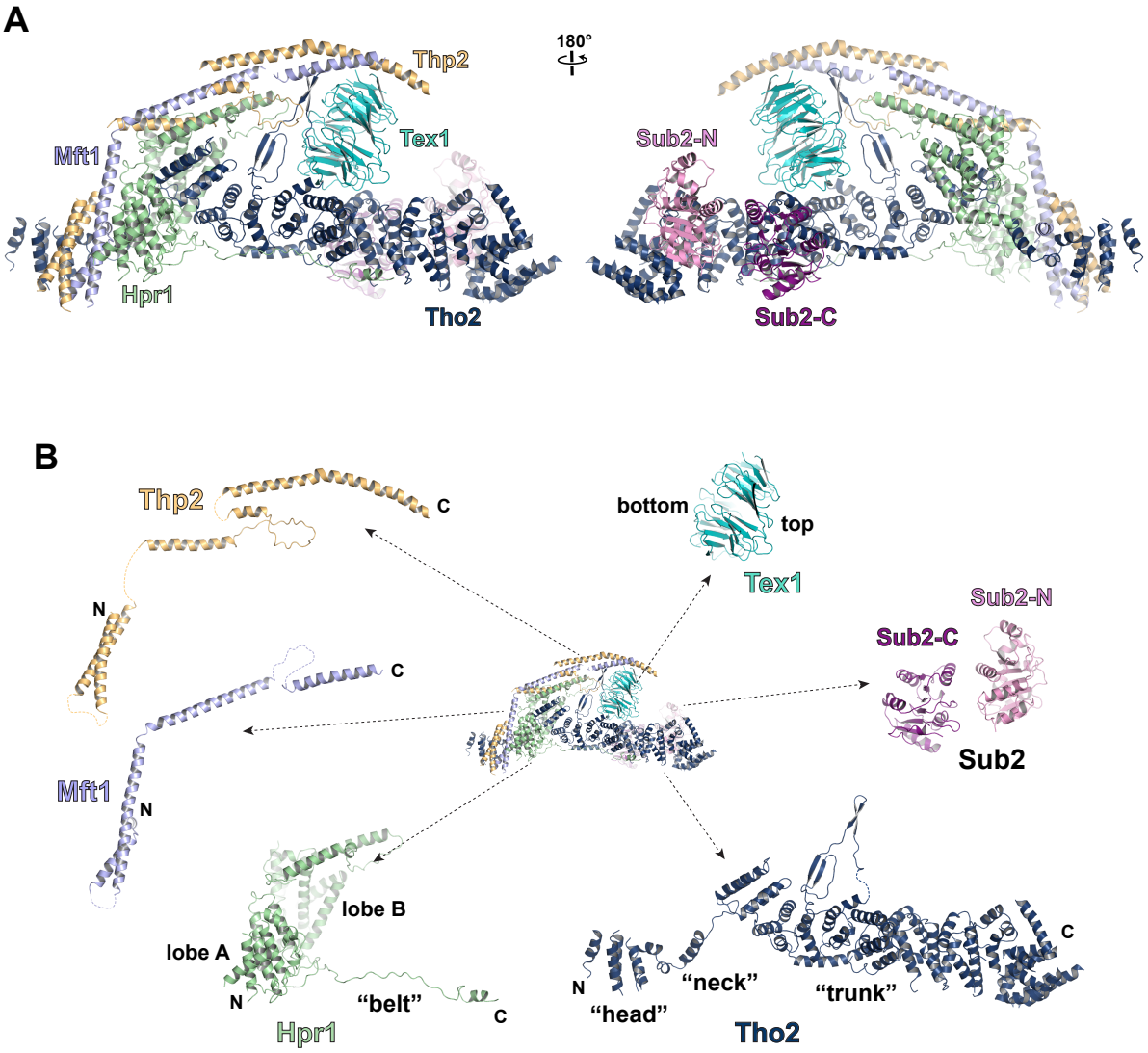

669 **Figure 2. Cryo-EM structure of the THO*•Sub2 complex at 3.70 Å resolution. A)**
670 Overall architecture of the THO*•Sub2 complex in front and back views. **B)** Dissected
671 view of the THO*•Sub2 complex subunits. The largest THO subunit, Tho2, contains a
672 "head", a "neck", and an α-solenoid "trunk". Hpr1 contains lobe A, lobe B, followed by an
673 extended "belt".

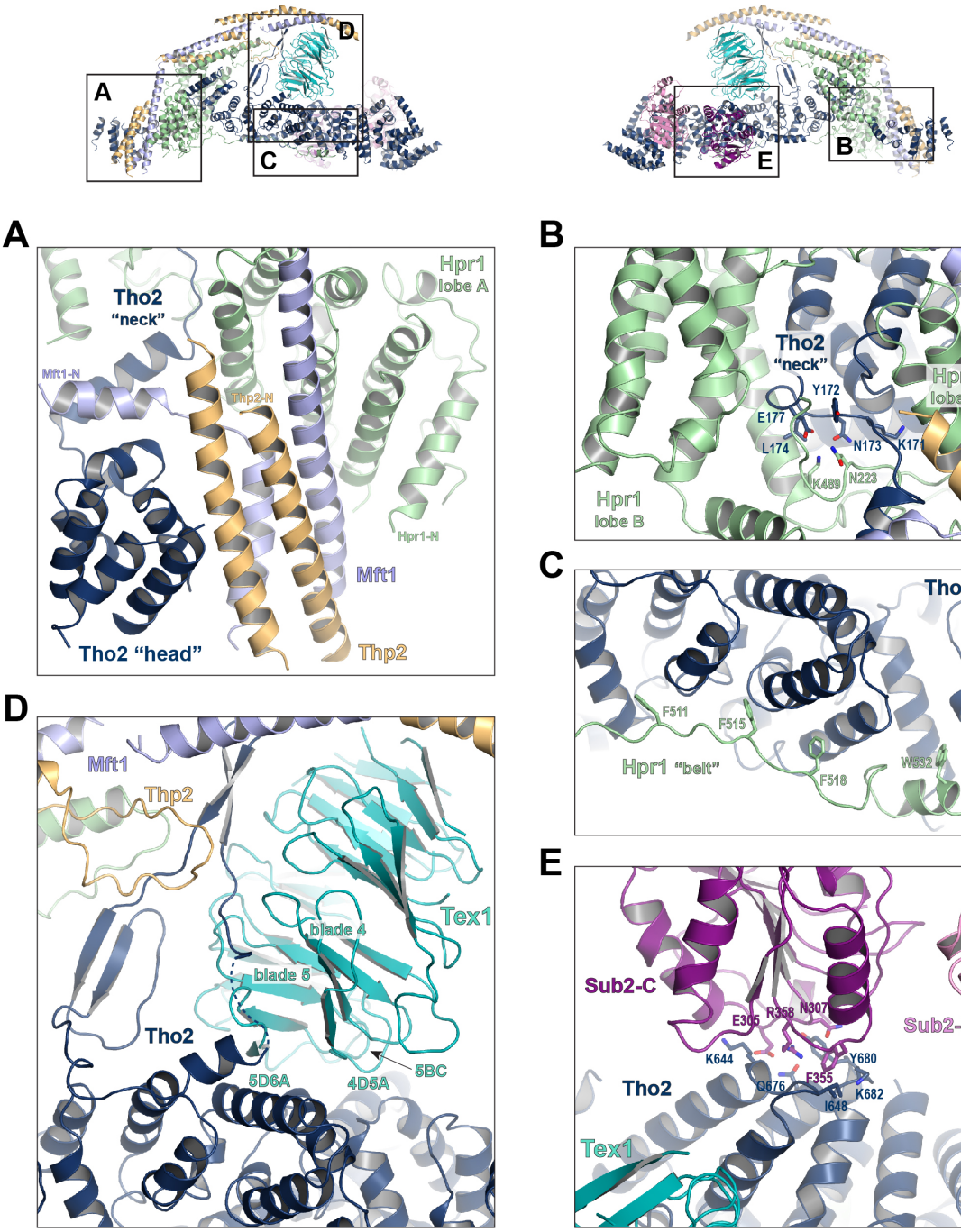

674 **Figure 3. Key interactions in the THO*•Sub2 complex. A)** A highly intimate interface
675 involving the Tho2 "head". **B)** The Tho2 "neck" is embraced by the two lobes of Hpr1. **C)**
676 The Hpr1 exhibits an extended "belt" lining the Tho2 "trunk". **D)** The Tex1 beta propeller
677 sits at the center of the Tho2 "trunk". **E)** The interface between Tho2 and Sub2-C.

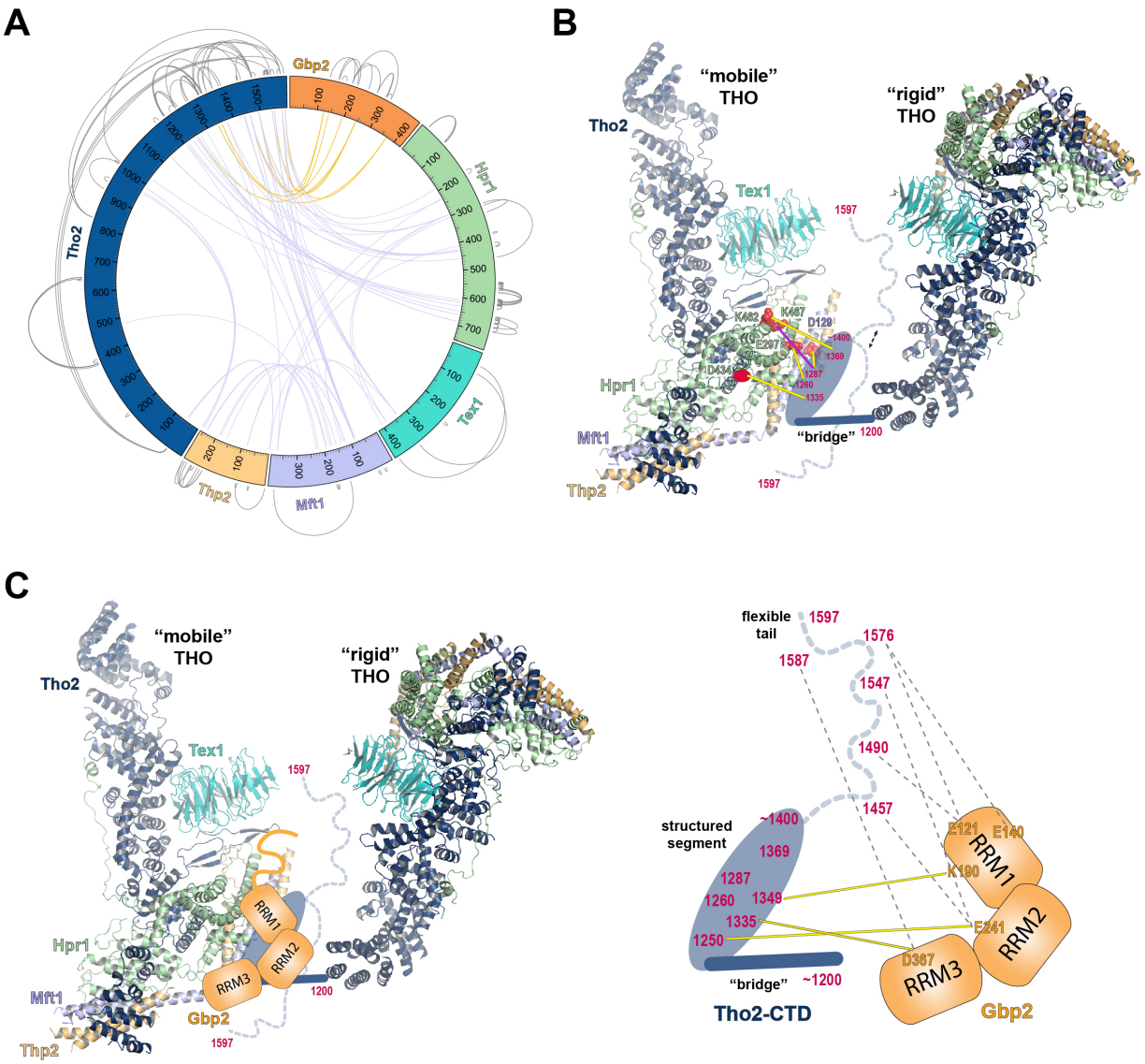

678 **Figure 4. Chemical cross-linking and mass spectrometry reveals THO-Gbp2**
679 **interactions. A)** Circular plot showing the intermolecular crosslinking sites with EDC
680 cross-linker. Each THO•Gbp2 complex subunit is represented as a colored segment with
681 the amino acid residues indicated. Inter-molecular crosslinks are mapped inside the circle
682 and the intra-molecular crosslinks are mapped outside the circle. The crosslinks between
683 Tho2 and Gbp2 are colored in orange. **B)** Schematics of the arrangement of the Tho2-
684 CTD, which contains a "bridge" connecting two THO molecules, followed by a structured
685 segment and a flexible tail (residues ~1400-1597). The EDC crosslinks between the
686 structured Tho2-CTD fragment and Hpr1 (E297, D434, and K462) as well as Mft1 (D129)
687 are indicated by yellow lines. The DSS crosslink between Tho2-CTD and Hpr1-K467 is
688 indicated by a purple line. **C)** Schematics of the THO-Gbp2 interactions (left) and the
689 identified crosslinking sites between Tho2-CTD and Gbp2 RRM domains. **D)** *In vitro* GST-
690 pull downs show that Gbp2 binds to the THO•Sub2 complex.
691

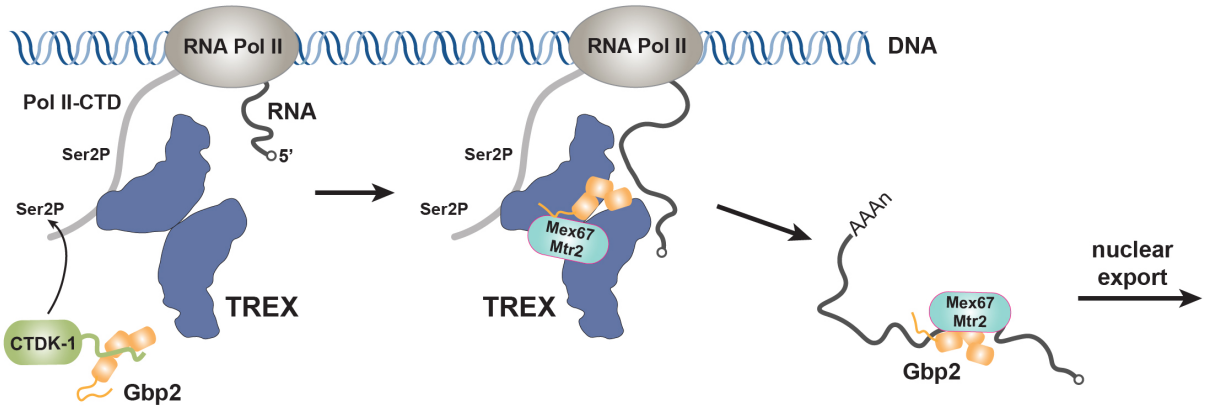

692 **Figure 5. Working model of coordinated function of TREX and Gbp2.**

693 During transcription, the yeast CTDK-1 complex phosphorylates Ser2 of the RNA Pol II
694 CTD. The N-terminal extension in CTDK-1's kinase subunit Ctk1 recognizes the RRM
695 domains of Gbp2, connecting Gbp2 to the transcription machinery. TREX travels along
696 with the transcription machinery and recognizes multiple domains of Gbp2, possibly
697 facilitating its loading onto the maturing mRNP. Both TREX and Gbp2 are involved in
698 subsequent loading of the export receptor Mex67•Mtr2 to generate export competent
699 mRNPs.

700

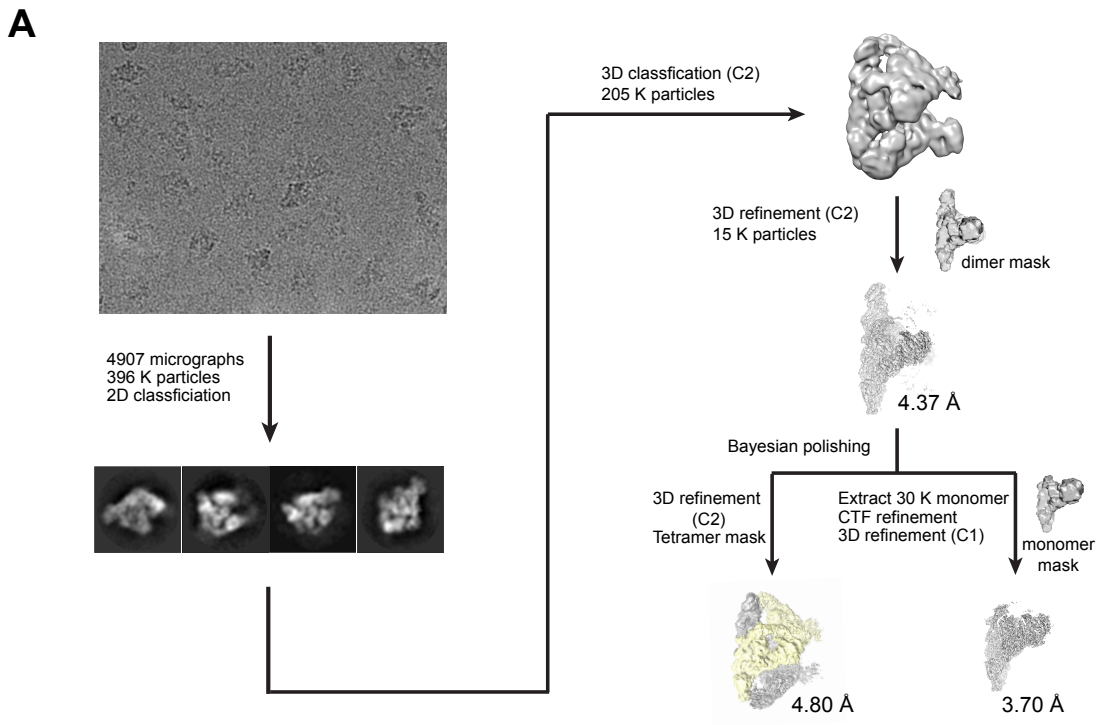

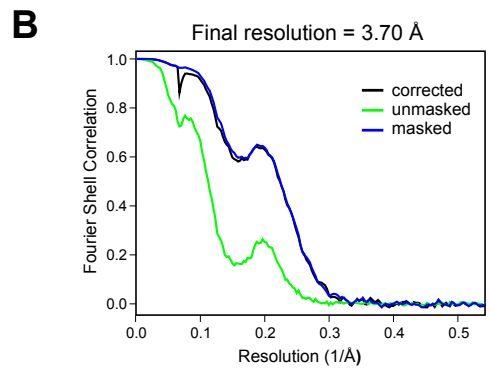

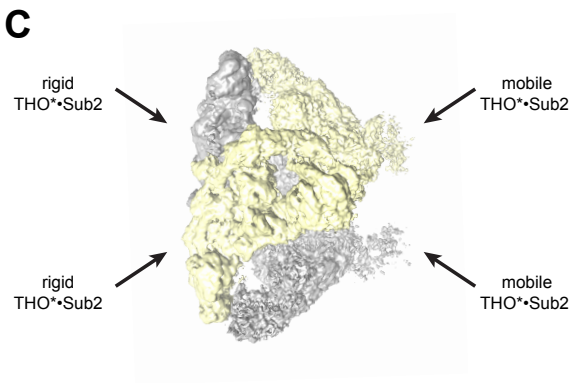

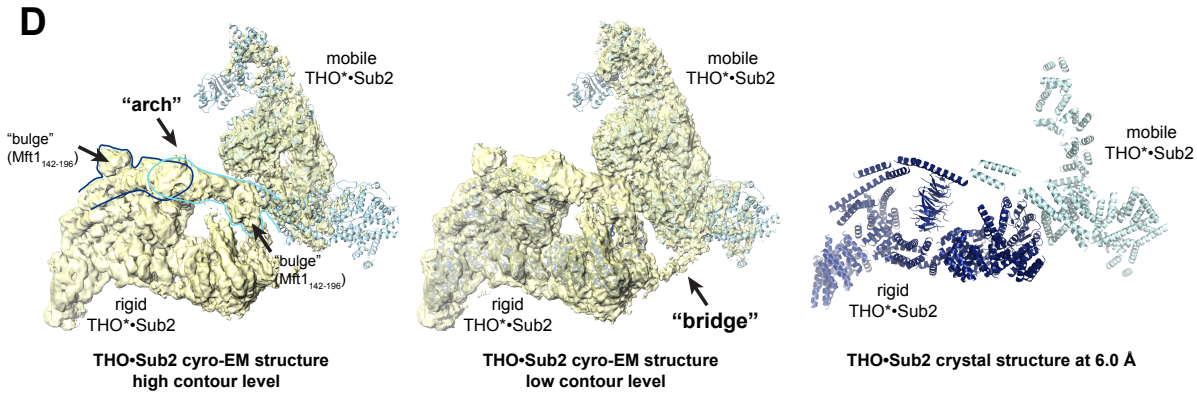

Figure 2-figure supplement 1. Cryo-EM data processing. A) Cryo-EM data processing workflow. **B)** Fourier shell correlation (FSC) curves between the two half maps of the THO*•Sub2 protomer. **C)** Individual particles of the cryo-EM sample contain four copies of the THO*•Sub2 protomer. **D)** An “arch” and a “bridge” are observed between a rigid THO*•Sub2 protomer and a mobile THO*•Sub2 protomer. Comparison of the cryo-EM map and our previous crystal structure (PDB ID 5SUQ) reveals that the crystal structure corresponds to a rigid THO*•Sub2 protomer and partial structure of a mobile THO*•Sub2 protomer.

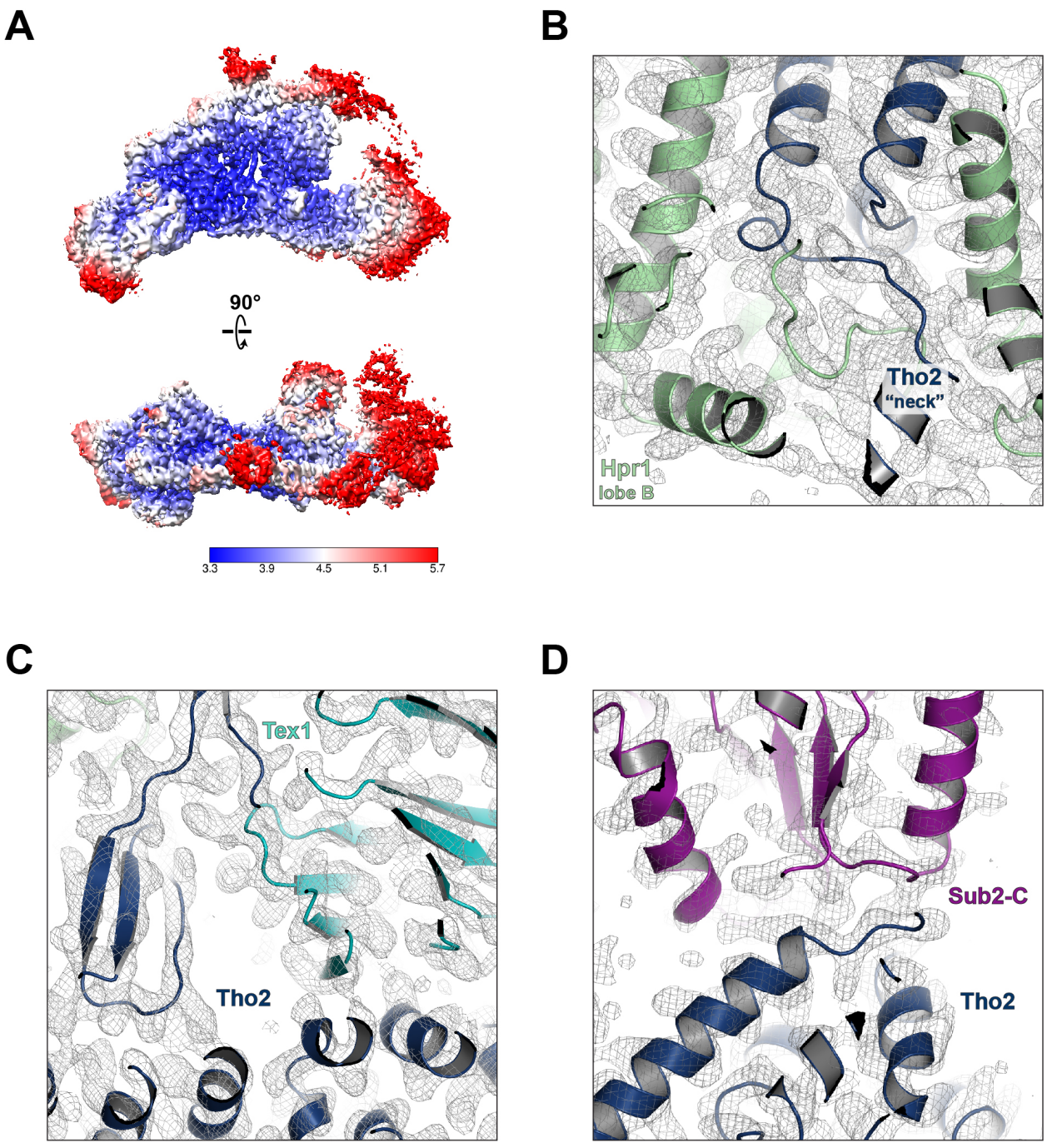

Figure 2-figure supplement 2. Cryo-EM model building. A) Local resolution of the final reconstruction calculated by Relion. Electron density maps at the Tho2 "neck" (**B**), the Tho2-Tex1 interface (**C**), and the Tho2-Sub2 interface (**D**).

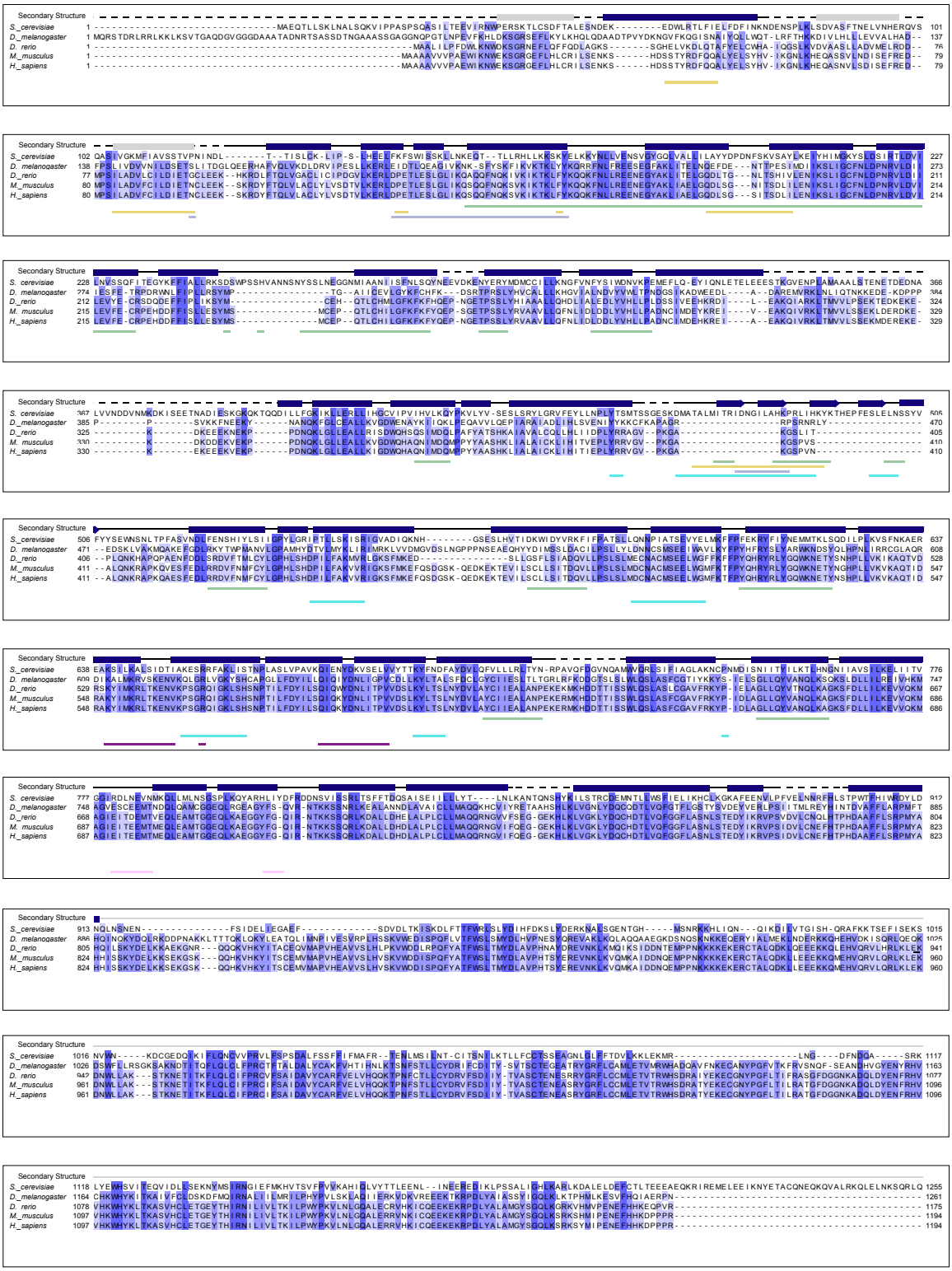

Figure 2-figure supplement 3. Sequence alignment of Tho2 homologues.

Tho2 sequences from *S. cerevisiae*, *D. melanogaster*, *D. rerio*, *M. musculus*, and *H. sapiens* were aligned with ClustalW. Shading indicates the degree of conservation across homologues. Tho2 secondary structural features from our cryo-EM structure are shown above the sequence alignment with α-helices represented as blue bars and β-sheets represented as blue arrows. The model of Tho2 contains ten poly-Ala helices at its C-terminus represented by gray line. Three poly-Ala helices at the N-terminus of Tho2 are represented by gray bars. Sequences that are not present in the model (loops and highly flexible regions) are represented by dotted lines. The regions of Tho2 that form interaction interfaces with each of the other THO Complex subunits were identified using PISA, and these interaction regions are shown below the sequence alignment. The coloration for the interaction regions is consistent with the color scheme throughout the manuscript with Hpr1 in green, Tex1 in cyan, Mft1 in light blue, Thp2 in yellow, Sub2-N in pink and Sub2-C in purple.

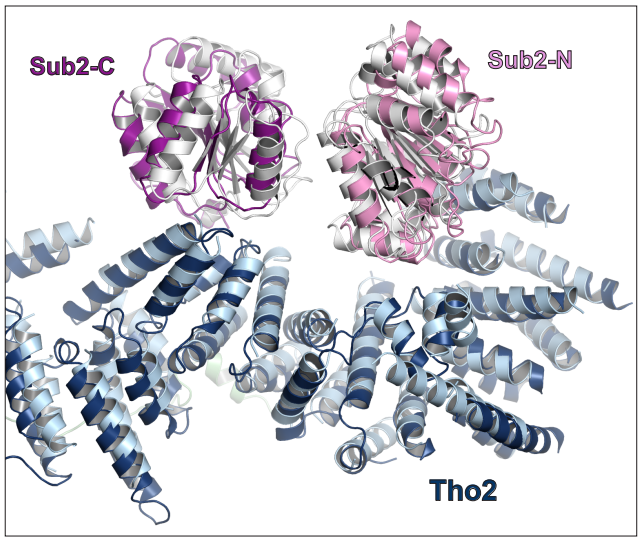

730

731 **Figure 3-figure supplement 1. Comparison of the cryo-EM structure and our**
732 **previous crystal structure of THO•Sub2 at the THO-Sub2 interface.** Cryo-EM
733 structure is colored in blue (Tho2), pink (Sub2-N), and purple (Sub2-C). Crystal structure
734 is colored in light blue (Tho2) and gray (Sub2-N and Sub-C).

735

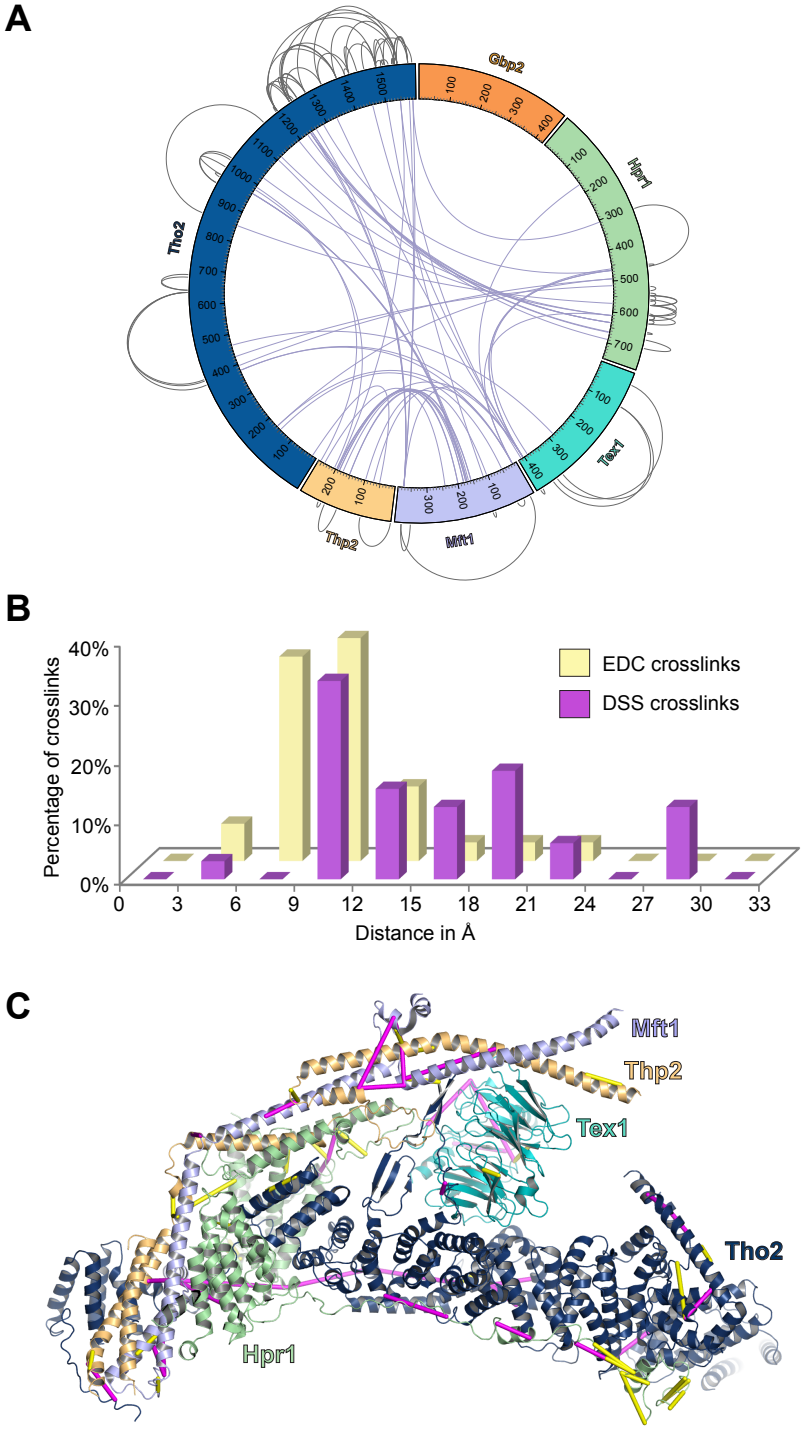

736 **Figure 4-figure supplement 1. Analyses of the XL-MS data. A)** Circular plot showing
737 the intermolecular crosslinking sites with DSS cross-linker. **B)** Distance distribution of the
738 crosslinks. We mapped the Cα-Cα distances between cross-linked residues onto the
739 dimeric THO structure (PDB ID 7AQO). 91% of the EDC crosslinks and 100% of the DSS
740 crosslinks that can be mapped to the structure fall within the expected threshold of 17 Å
741 and 30 Å. **C)** EDC (yellow) and DSS (purple) crosslinks are mapped on the THO structure
742 (PDB ID 7APX).

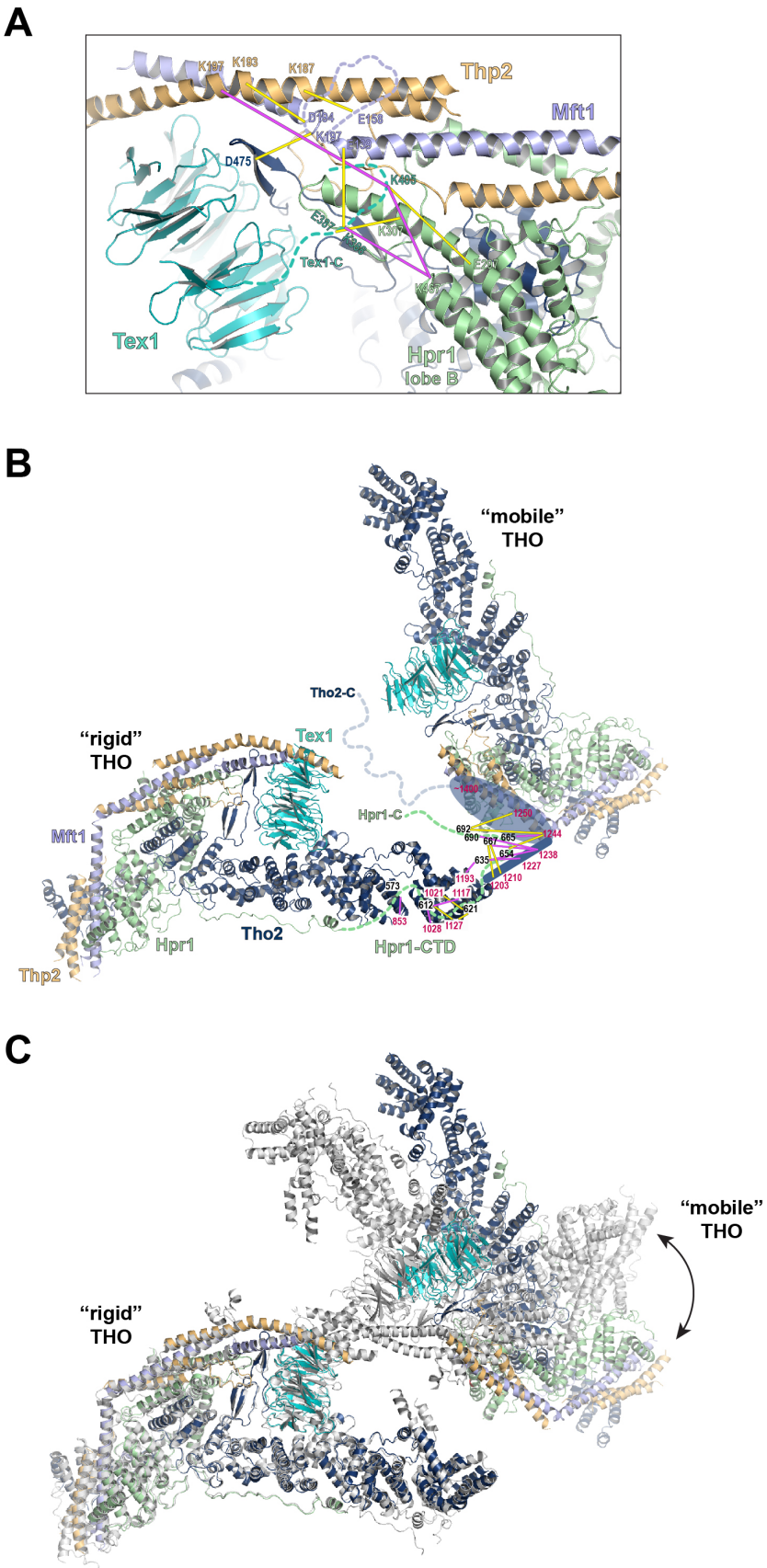

743 **Figure 4-figure supplement 2. XL-MS data indicate the arrangement of the C-termini**
744 **of Tex1 and Hpr1. A)** The C-terminal tail of Tex1 (residues 367-422) is localized near
745 Hpr1 lobe B. The crosslinking sites are indicated by yellow lines. **B)** The Hpr1-CTD binds
746 to the C-terminus of the Tho2 “trunk” and is localized close to the neighboring THO
747 molecule. **C)** Structural alignment of the dimeric THO assembly between our cryo-EM
748 structure and the recently reported THO-Sub2 structure (PDB ID 7AQO). Sub2 is omitted
749 for clarity. The structures are aligned using one THO molecule, revealing significant
750 flexibility in the relative orientation between the two THO molecules.

Table 1. Cryo-EM data collection, refinement and validation statistics

	THO-Sub2 protomer (EMDB-xxxx) (PDB xxxx)	THO-Sub2 tetramer (EMDB-xxxx)
Data collection and processing		
Microscope/Camera	Titan Krios/Falcon 3EC	
Voltage (kV)	300	
Electron exposure (e–/Å^2)	50	
Defocus range (μm)	0.8 to 2.0	
Pixel size (Å)	0.681	
Symmetry imposed	C1	
Initial particle images (no.)	396 K	
Final particle images (no.)	30 K	15 K
Resolution at 0.143 FSC (masked, Å)	3.70	4.80
Map sharpening *B* factor (Å^2)	86	145
Refinement		
Model resolution at 0.5 FSC (Å)	3.87	
Model composition		
Protein residues	2378	
B factors (Å^2)		
Protein	109.6	
R.m.s. deviations		
Bond lengths (Å)	0.008	
Bond angles (°)	1.11	
Validation		
MolProbity score	2.14	
Clashscore	11.86	
Poor rotamers (%)	0.15	
Ramachandran plot		
Favored (%)	90.1	
Allowed (%)	9.7	
Disallowed (%)	0.2	